

Supporting Information for:

Noninterleaved Metasurface for (2⁶-1) Spin- and Wavelength-Encoded Holograms

Lei Jin^{1,1}, Zhaogang Dong^{2,1}, Shengtao Mei¹, Ye Feng Yu³, Zhun Wei¹, Zhenying Pan^{2,3}, Soroosh Daqiqeh Rezaei^{4,2}, Xiangping Li⁵, Arseniy I. Kuznetsov^{2,3}, Yuri S. Kivshar⁶, Joel K. W. Yang^{7,2,*}, and Cheng-Wei Qiu^{1,*}

¹Department of Electrical and Computer Engineering, National University of Singapore, 4 Engineering Drive 3, Singapore 117583, Singapore

²Institute of Materials Research and Engineering, A*STAR (Agency for Science, Technology and Research), 2 Fusionopolis Way, #08-03 Innovis, 138634 Singapore

³Data Storage Institute, A*STAR (Agency for Science, Technology and Research), 2 Fusionopolis Way, #08-01 Innovis, 138634 Singapore

⁴Department of Mechanical Engineering, Faculty of Engineering, National University of Singapore, 9 Engineering Drive 1, 117575, Singapore

⁵Guangdong Provincial Key Laboratory of Optical Fiber Sensing and Communications, Institute of Photonics Technology, Jinan University, Guangzhou, 510632 China

⁶Nonlinear Physics Centre, Australian National University, Canberra ACT 2601, Australia

⁷Singapore University of Technology and Design, 8 Somapah Road, 487372 Singapore

*Corresponding authors: Cheng-Wei Qiu (email: chengwei.qiu@nus.edu.sg; telephone: +65 65162559;) and Joel K. W. Yang (email: joel_yang@sutd.edu.sg; telephone: +65 64994767).

S1. Material properties used for the simulation

Figure S1 shows the measured refractive index of amorphous Si used in this work.

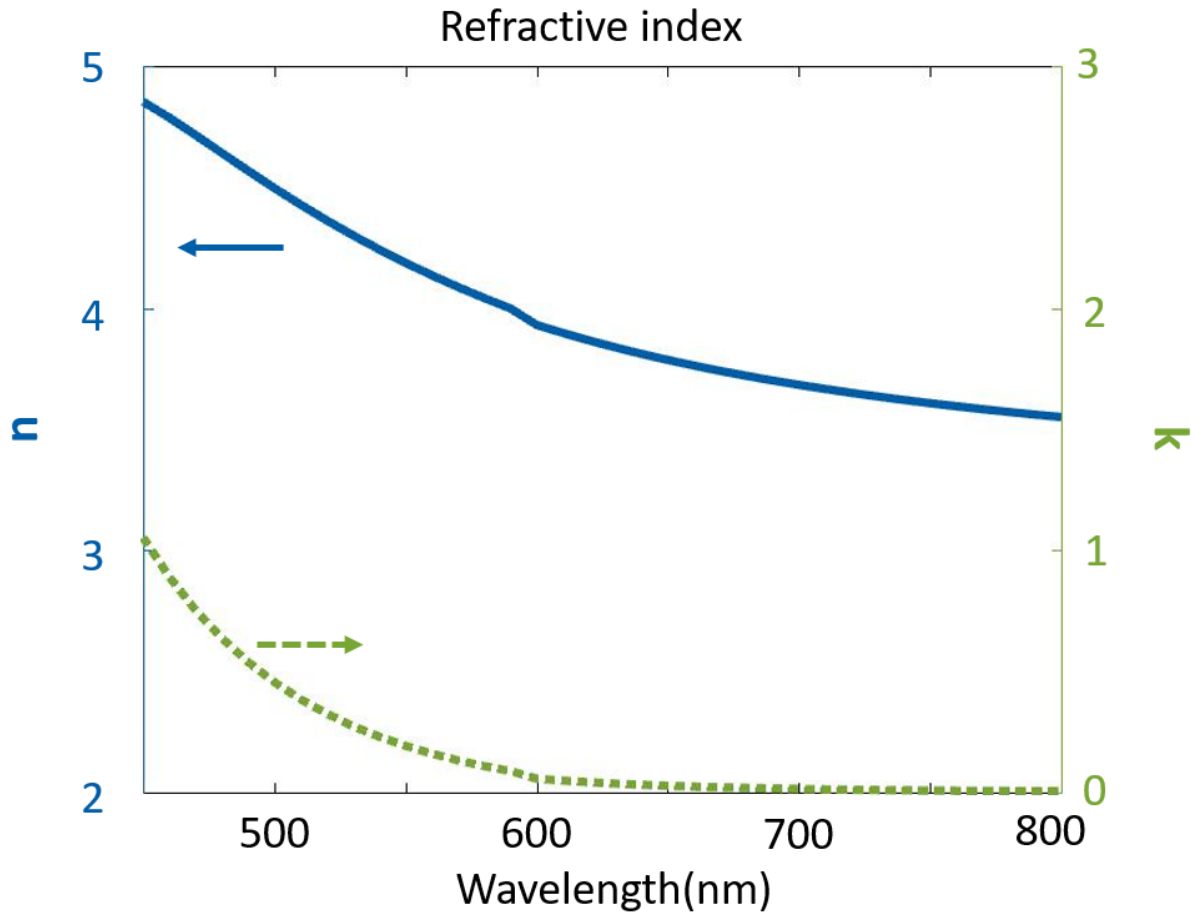


Figure S1. Refractive index of amorphous Si. Measured real (blue solid curve) and imaginary (green dash curve) parts of the refractive index (n and k) as a function of wavelength.

S2. PB phase introduced by nanobrick

The single nanobrick is an anisotropic scatterer. Then, the Jones matrix for this nanobrick with the in-plane orientation θ can be expressed as⁽¹⁾

$$T(\theta) = R(-\theta)T_0R(\theta) = R(-\theta) \begin{bmatrix} t_l & 0 \\ 0 & t_s \end{bmatrix} R(\theta). \quad (1)$$

where t_l and t_s are the complex transmission coefficients for incident light linearly polarized along the long or short axes of the nanobrick, respectively; $R(\theta)$ is the rotate matrix.

From Eq. (1) we can deduce the expression of the transmission field:

$$E_t = T(\theta)E_i = T(\theta) \begin{bmatrix} 1 \\ \pm i \end{bmatrix} = \frac{t_l+t_s}{2} \begin{bmatrix} 1 \\ \pm i \end{bmatrix} + \frac{t_l-t_s}{2} e^{i2(\pm\theta)} \begin{bmatrix} 1 \\ \mp i \end{bmatrix}, \quad (2)$$

where \pm correspond to right- (RCP) and left-circularly polarized (LCP) beam, respectively. Therefore, a silicon nanobrick with a rotating angle will introduce the geometric phase $\pm 2\theta$ for opposite spins. The ratio between the optical power of the transmitted light with opposite spins and the incident optical power is defined as conversion efficiency, which is calculated by $(t_l - t_s)/2$. The numerical demonstrations of phase changes for the RCP incident beam are shown in Fig. S2.

According to Eq. (2), the conversion efficiency is restrained by the magnitudes and phases of the complex transmission coefficients t_l and t_s which are defined by $\vec{E}_t^{l/s}/\vec{E}_i^{l/s}$. The transmission field can be expressed as $\vec{E}_t^{l/s} = \vec{E}_i^{l/s} + \vec{E}_{sca}^{l/s}$, where $\vec{E}_{sca}^{l/s}$ is the scattered field of induced multipole by the Si nanobricks. Therefore, to achieve the conversion efficiency, the detailed optical characteristics of the Si nanobrick are analyzed.

Here we use the Cartesian multipole analysis to calculate the response the Si nanobrick array with same orientation⁽²⁾⁻⁽⁴⁾. Figure S3 shows the simulated optical responses for the incident beam with linear polarization along long-axis (a, b, c) and short-axis (d, e, f) of Si nanobrick.

Multipole decomposition is performed, showing that the electric dipole (ED) and magnetic dipole (MD) modes are excited in the Si nanobricks, as shown in Fig. S3 (a, d) with the corresponding phases of ED and MD shown in Fig. S3 (b, e). Figures S3 (c, f) show the amplitudes and phase changes of the simulated transmission. These simulations demonstrate that there is a different response to the incident beam with linear polarization along long-axis and short-axis of the Si nanobrick. When the polarization of incident beam is along long-axis of the Si nanobrick, the magnitude of \vec{E}_{sca}^l is comparable to that of \vec{E}_i^l , which causes \vec{E}_t^l to be sensitive to the amplitude and phase of the ED and MD. When the ED and MD have equal amplitude and the phase difference of π , the second Kerker condition^{(4),(5)} is fulfilled resulting in the transmission dip. Moreover, due to the compositions of the ED and incident beam, the phase changes of \vec{E}_t^l are inversely proportional to wavelength, where some fluctuations are observed near 600 nm because of the effect of MD. However, when the polarization of incident beam is changed to short-axis, the magnitude of \vec{E}_{sca}^s is far below that of \vec{E}_i^s , which causes the small dip of transmission and a less phase change of \vec{E}_t^s . The aforementioned magnitudes and phases of t_l and t_s provide two peaks of conversion efficiency as shown in Fig. S3 (g).

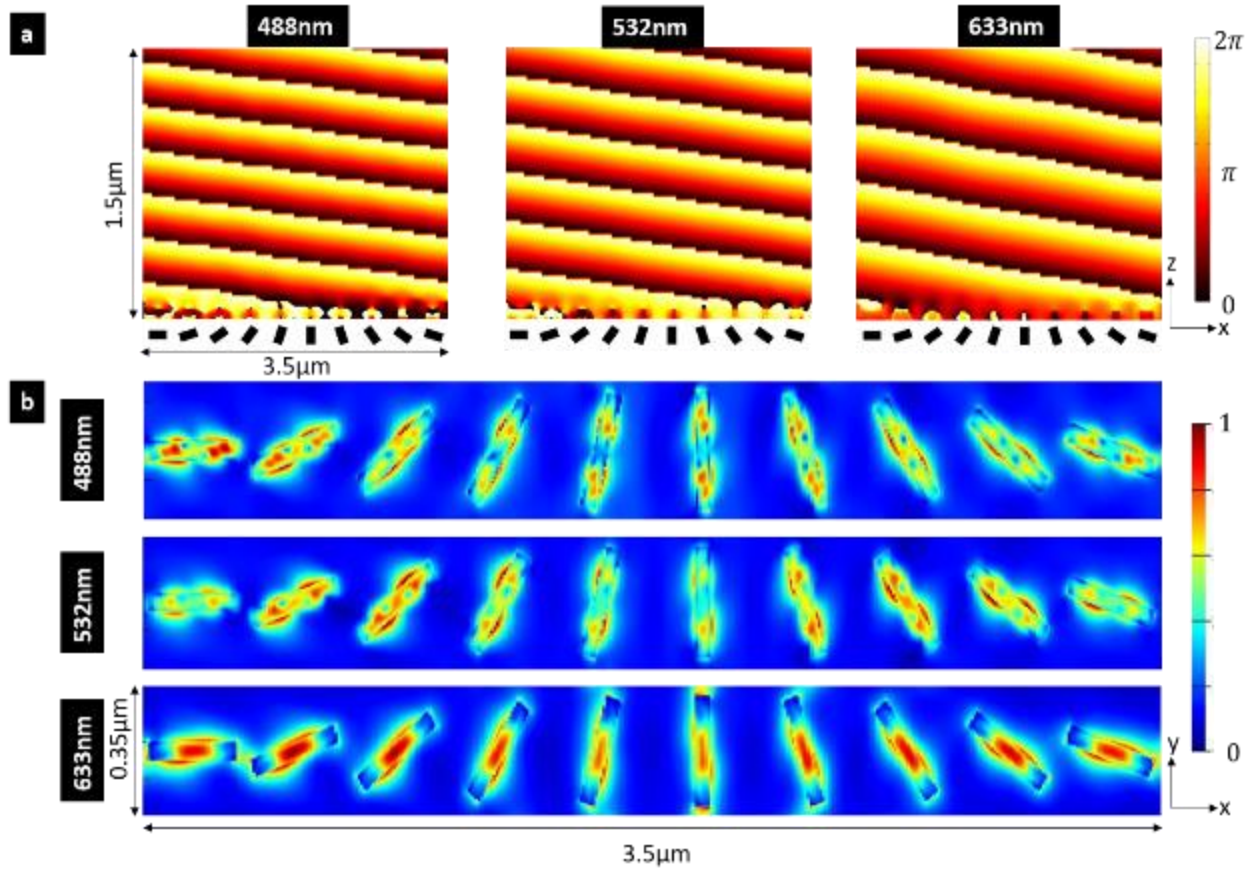


Figure S2. Simulation results of a periodic Si nanobrick array. (a) Phase profiles of transmitted light with opposite spins through a periodic Si nanobrick array varying with in-plane orientation angle (from 0° to 162° with an equal interval of 18°) along x in one period. The plane wave with circular polarization incident from the z -direction and the working wavelength is selected as 488 (left), 532 (middle) and 633 nm (right) sequence. All phase profiles from $z = 0$ (where the bottom surface of the nanobrick is located) to $z = 1.5 \mu\text{m}$ show tilting phase profiles, implying that the transmitted lights have additional gradient phases introduced by Si nanobricks with the in-plane orientation angle varying. Because the introduced geometric phases are wavelength-independent, the tilting angles are increased with increasing working wavelength. (b) Top views of power distributions of a periodic Si nanobrick array at plane $z = 0.5h$ for 488 (top), 532 (middle) and 633 nm (bottom) sequence.

633 nm (bottom). All power distributions show that the power is strongly confined around the nanobricks.

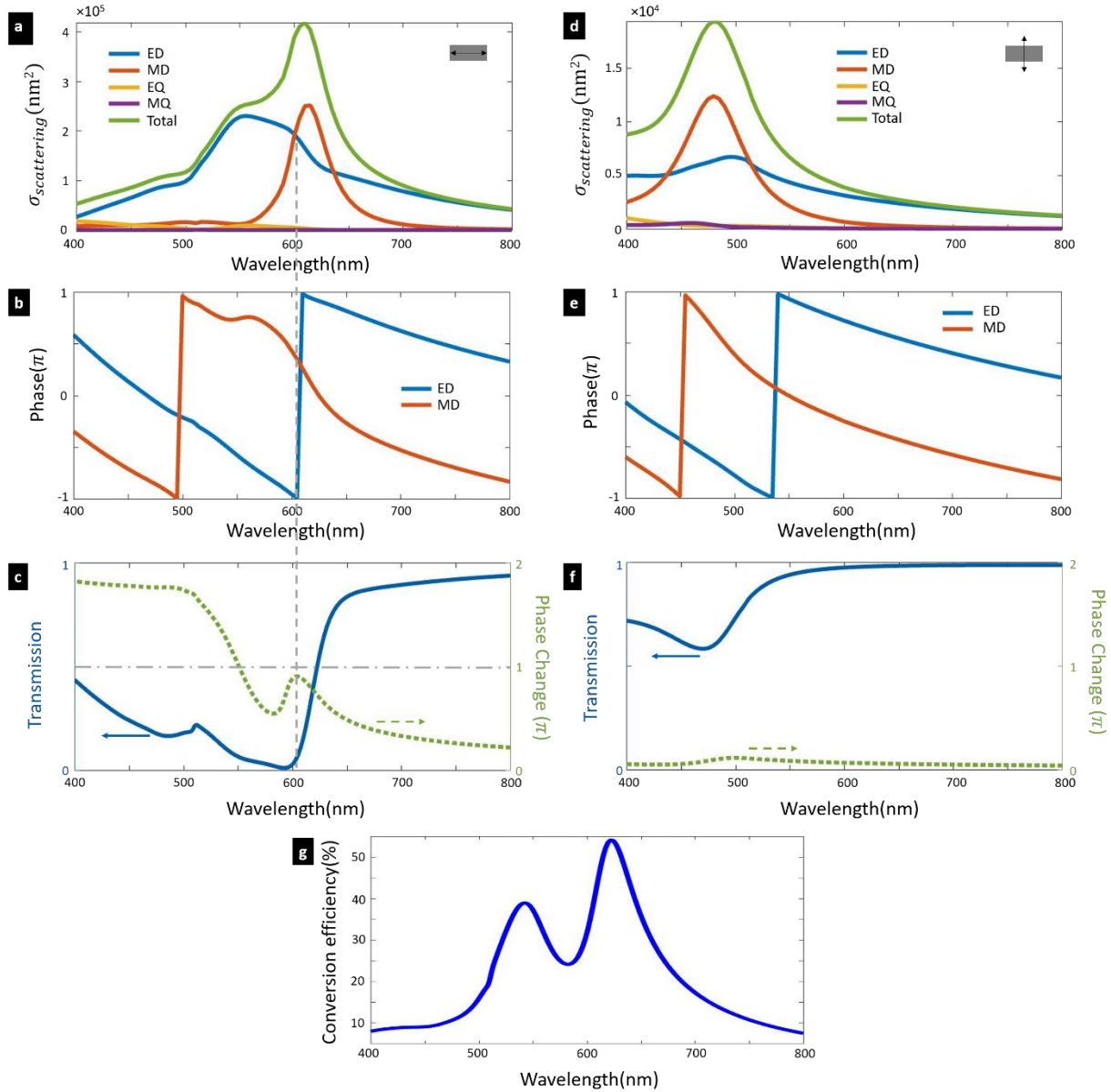


Figure S3. Optical characteristics of the Si nanobrick array with same orientations. Optical responses to the incident beams with linear polarization along long-axis (a, b, c) and short-axis (d, e, f) of the nanobrick. (a, d) Multipole decomposition calculations of the scattering cross sections, $\sigma_{\text{scattering}}$, for the ED, MD, MQ and EQ modes. Inset: Gray rectangle is a nanobrick and double arrow is the polarization of incident beam. (b, e) Individual phases of the excited ED and MD, as

retrieved from the multipolar decomposition. (c, f) The amplitudes and phase changes of the simulated transmission. (g) Simulated conversion efficiency. The conversion efficiency is defined as the ratio between the optical power of the transmitted light with opposite handedness and the incident optical power, which is calculated by $(t_l - t_s)/2$.

S3. Dispersion relationship

The phase function $\varphi(x_0, y_0)$ of metasurface is defined by the in-plane orientations of the nanobrick array, which means that the designed metasurface is able to provide the same phase profile for different incident wavelengths. When a beam illuminates this metasurface, the E-field distribution of transmission wave is $U_0(x_0, y_0) = e^{i\varphi(x_0, y_0)}$. The diffraction field in Fresnel zone can be calculated by the Fresnel diffraction expression.

$$U(x, y) = \frac{1}{i\lambda z} e^{ikz} \iint_{-\infty}^{+\infty} U_0(x_0, y_0) e^{i\frac{k}{2z}[(x-x_0)^2 + (y-y_0)^2]} dx_0 dy_0. \quad (3)$$

If we consider the E-field intensity distribution, the Eq. (3) can be rewritten as

$$|U(x, y)| = \left| \frac{1}{i\lambda z} \right| |e^{ikz}| \left| \iint_{-\infty}^{+\infty} U_0(x_0, y_0) e^{i\frac{\pi}{\lambda z}[(x-x_0)^2 + (y-y_0)^2]} dx_0 dy_0 \right|. \quad (4)$$

According to Eq. (4), for the phase-modulated meta-hologram, the same phase profiles at different wavelengths will provide the same $U_0(x_0, y_0)$. Because $|e^{ikz}| = 1$, when λz equal to a constant, we will achieve the same E-field intensity distribution. Therefore, for a given metasurface formed by nanobricks to realize a meta-hologram, the different wavelength beams are able to reconstruct same images at different distances.

S4. Multi-wavelength Gerchberg-Saxton algorithm

As shown in Fig. S4, this multi-wavelength Gerchberg-Saxton algorithm^{(6),(7)} is a serial iterative algorithm. Because the amplitude of the target image has 3 parts for red, green and blue light, every loop is formed by 3 steps. Each step corresponds to one given wavelength and consists of Fresnel diffraction, replacement of amplitude at the observation plane, inverse Fresnel diffraction, and normalization at the metasurface plane. As a result, we can get an optimized phase-only hologram, which enables the reconstruction of multi-color images at the given z -plane.

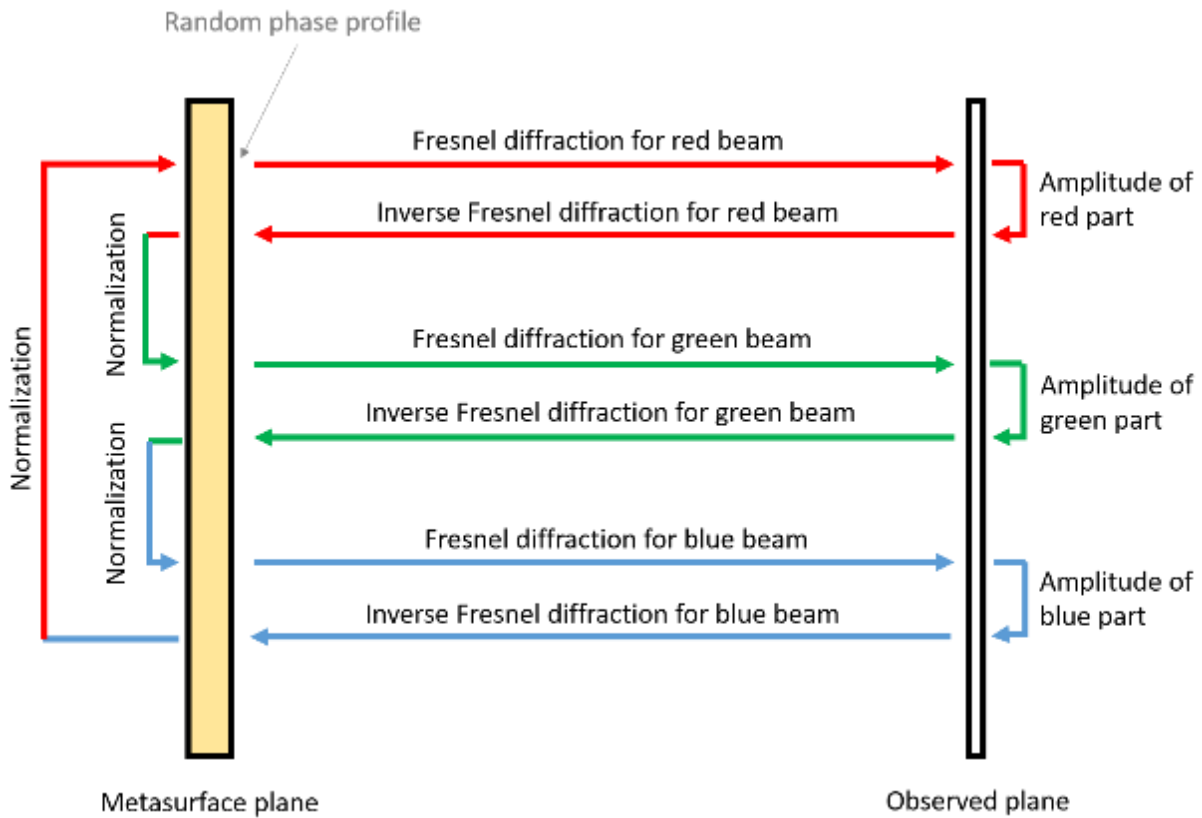


Figure S4. Flow chart of the multi-wavelength Gerchberg-Saxton algorithm. This loop is formed by 3 steps labelled by red, green and blue colours, which represent the phase retrieval for red, green and blue light, respectively. Each step corresponds to one given wavelength and consists of Fresnel diffraction, replacement of amplitude at the observation plane, inverse Fresnel diffraction, and normalization at the metasurface plane.

S5. Detailed illustration of phase profiles.

Figure S5 shows the detailed illustration of the phase profiles $\varphi_{RCP}(x_0, y_0)$ and $\varphi_{LCP}(x_0, y_0)$. These two phase profiles reconstruct real image at observation plane for the incident light with RCP and LCP, respectively. The first phase profiles $\varphi_{RCP}(x_0, y_0)$ (shown in Fig. S5 (a)) reconstructs letters “B”, “G” and “R” at the distances Zr_B, Zr_G and Zr_R for the red incident light. Similarly, $\varphi_{RCP}(x_0, y_0)$ reconstructs these letters at Zg_B, Zg_G and Zg_R for the green incident light (or at Zb_B, Zb_G and Zb_R for the blue incident light). According to the distance condition in Supporting Information Section 2, the relationship of those distances should be $Zr_B < Zg_B < Zb_B$, $Zr_G < Zg_G < Zb_G$ and $Zr_R < Zg_R < Zb_R$. By carefully designing the distances, the equation, $Zr_R = Zg_G = Zb_B = Z_0$, can be realized. Hence, the three different images can be reconstructed in the observation plane (at Z_0) for the red, green and blue incident lights. Using the same method, as shown in shown in Figure S5 (b), the second phase profile $\varphi_{LCP}(x_0, y_0)$ reconstructs “flower”, “leaf” and “snowflake” patterns at the observation plane for the red, green and blue incident beams. Then, the function $Ae^{i\varphi(x_0, y_0)} = e^{i\varphi_{RCP}(x_0, y_0)} + e^{i\varphi_{LCP}(x_0, y_0)}$ is used to merge these two phase profiles together. The reconstructed images of the merged phase profile are shown in Fig. S6 and Fig. S7 for the incident light with RCP and LCP, respectively.

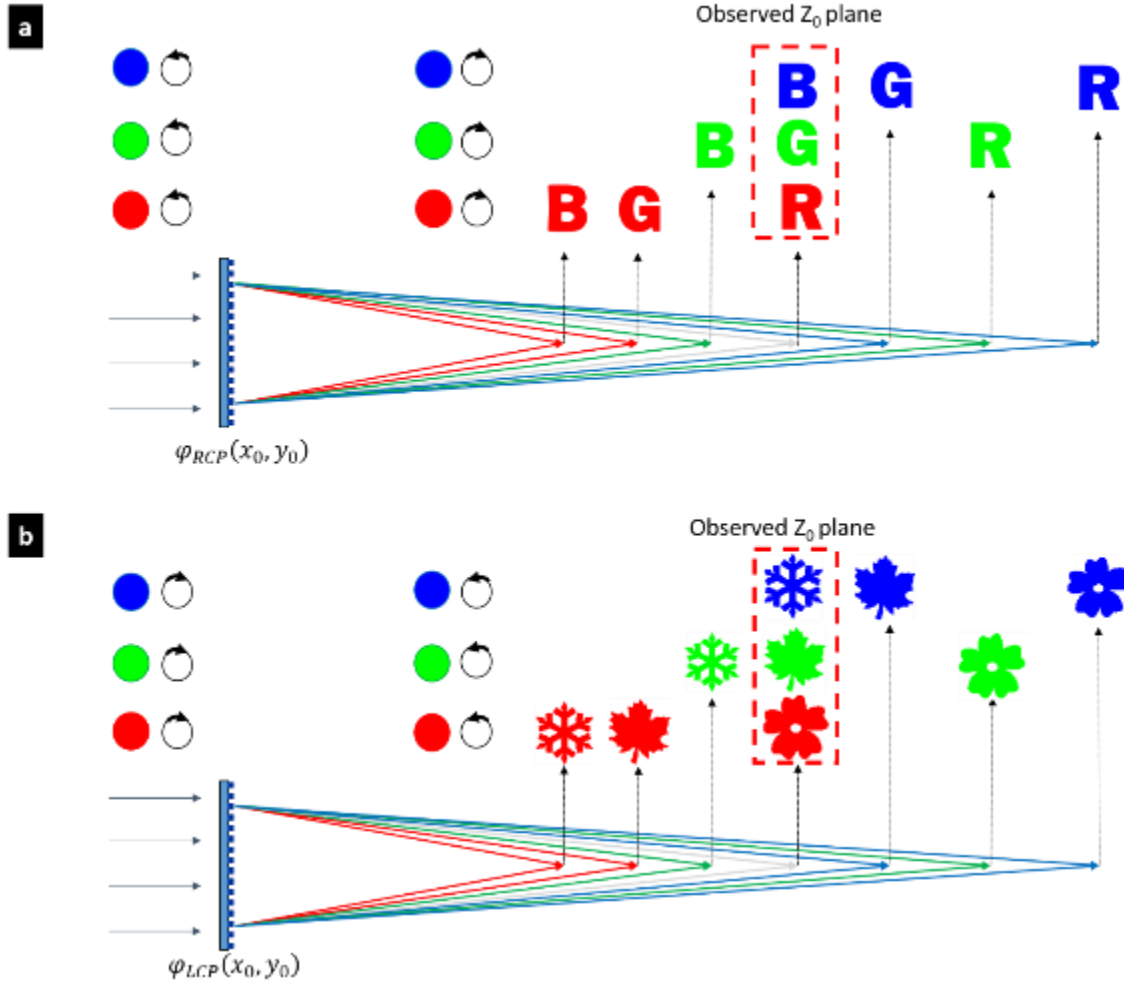


Figure S5. Detailed illustration of phase profiles $\varphi_{RCP}(x_0, y_0)$ and $\varphi_{LCP}(x_0, y_0)$. The polarization states of the incident light are chosen to be (a) RCP for phase profile $\varphi_{RCP}(x_0, y_0)$ and (b) LCP for phase profile $\varphi_{LCP}(x_0, y_0)$. The phase profiles $\varphi_{RCP}(x_0, y_0)$ reconstructs letters “B”, “G” and “R” at the distances Zr_B , Zr_G and Zr_R for the red incident light, respectively. According to the dispersion relationship, the distances are increased with reducing working wavelength. By carefully designing the distances, the phase profile $\varphi_{RCP}(x_0, y_0)$ reconstructs “R”, “G” and “B” patterns at the observation plane for the red, green and blue incident RCP beams. Using the same method, the second phase profile $\varphi_{LCP}(x_0, y_0)$ reconstructs “flower”, “leaf” and “snowflake” patterns at the observation plane for the red, green and blue incident LCP beams.

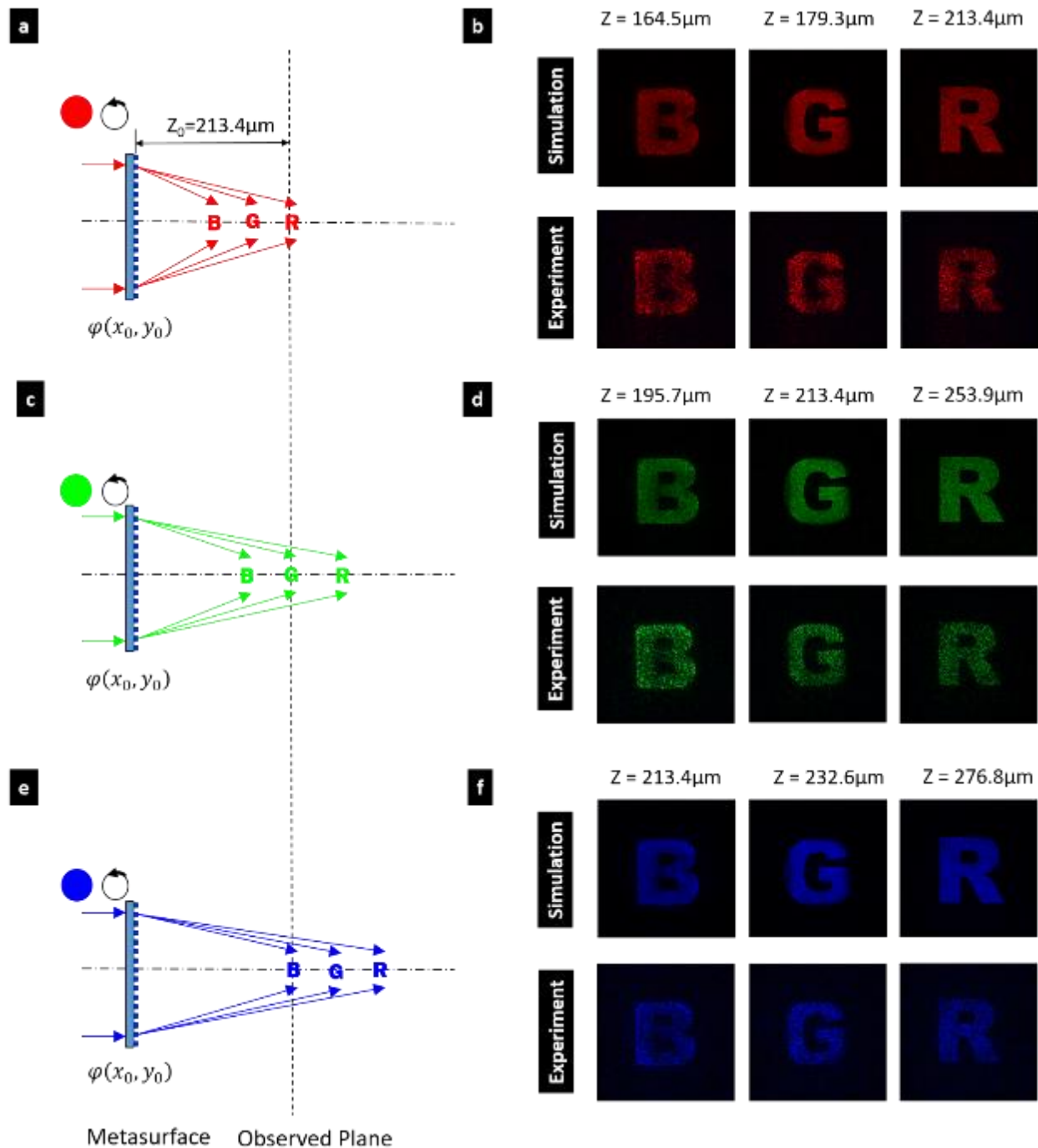


Figure S6. Reconstructed images by the right-circularly polarized (RCP) beams for different wavelengths. The wavelength of incident light is 633 (a, b), 532 (c, d) and 488 nm (e, f). (a, c, e): schematic illustration of the metasurface. (b, d, f): simulated (top) and measured (bottom) intensity profiles. Z_0 denotes the distance between the metasurface and reconstructed image plane.

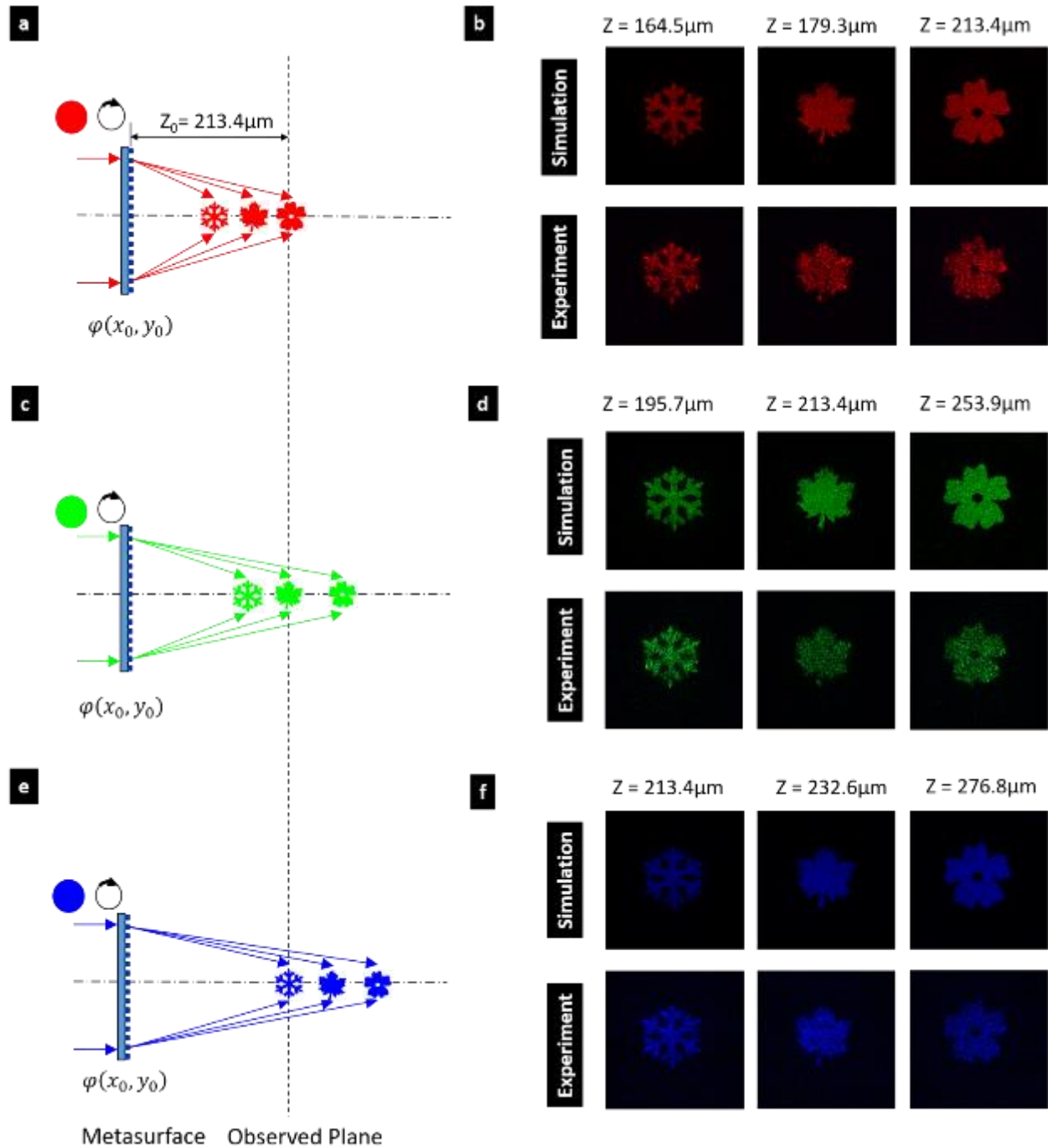


Figure S7 . Reconstructed images by the left-circularly polarized (LCP) beams for different wavelengths. The wavelength of incident light is 633 (a, b), 532 (c, d) and 488 nm (e, f). (a, c, e): schematic illustration of the metasurface. (b, d, f): simulated (top) and measured (bottom) intensity profiles. Z_0 denotes the distance between the metasurface and reconstructed image plane.

S6. Experimental setup for characterization of the spin and wavelength multiplexed Si hologram.

The schematic diagram of the experimental setup for the holographic reconstruction is shown in Fig. S8 (a). Here, three lasers, emitting at 488, 532 and 633 nm, are used. After being collimated by lenses, L1, L2 and L3, respectively, these laser beams from the fibers are combined together with two beam splitters (BSs) and directed onto the sample. There are three iris diaphragms (ID1, ID2 and ID3) after these three collimated beams respectively, which are applied as optical switches to control the incident beam. According to the wavelength of incident beam, a wide-band linear polarizer (P1) and a quarter-wave plate (QWP1) operating at the given wavelength are chosen to work as a circular polarizer. By controlling the angle between the polarization axis of P1 and the fast axis of QWP1, the polarization state of incident beam is tuned. The circularly polarized beam is normally incident on the hologram. The reconstructed images are formed by collecting the transmitted spin-inversed beams using a $\times 50$ objective lens (NA=0.60), then filtered by another circular polarization analyzer (P2 and QWP2), and finally captured by a CCD camera.

S7. Experimental setup for characterization of the 6-bit Metasurface.

To arbitrarily combine the 6 fundamental bases of the input beams, we modified the experiment setup as shown in Fig. S8 (b). We now place three polarizers (P1, P2 and P3) and three half-wave plates (HWP1, HWP2, and HWP3) after the collimated lenses, respectively. The Ps and HWPs are used to individually control the polarization direction of the laser beams with three primary colours. After being combined by the two beam splitters, the combined beams pass through the achromatic QWP to change the polarization from linear polarization (LP) to RCP, LCP or LP according to the rotation angles of the fast axis of the HWPs. The arbitrary combination of 6 fundamental bases is realized by tuning the rotation angles of the HWPs and controlling the IDs. The reconstructed images are collected by an objective lens and recorded by a CCD camera. Compared with the previous setup (shown in Fig. S8 (a)), a broadband QWP is used and the circular polarization analyzer before the CCD camera is removed, which introduces additional noise to the holographic projections.

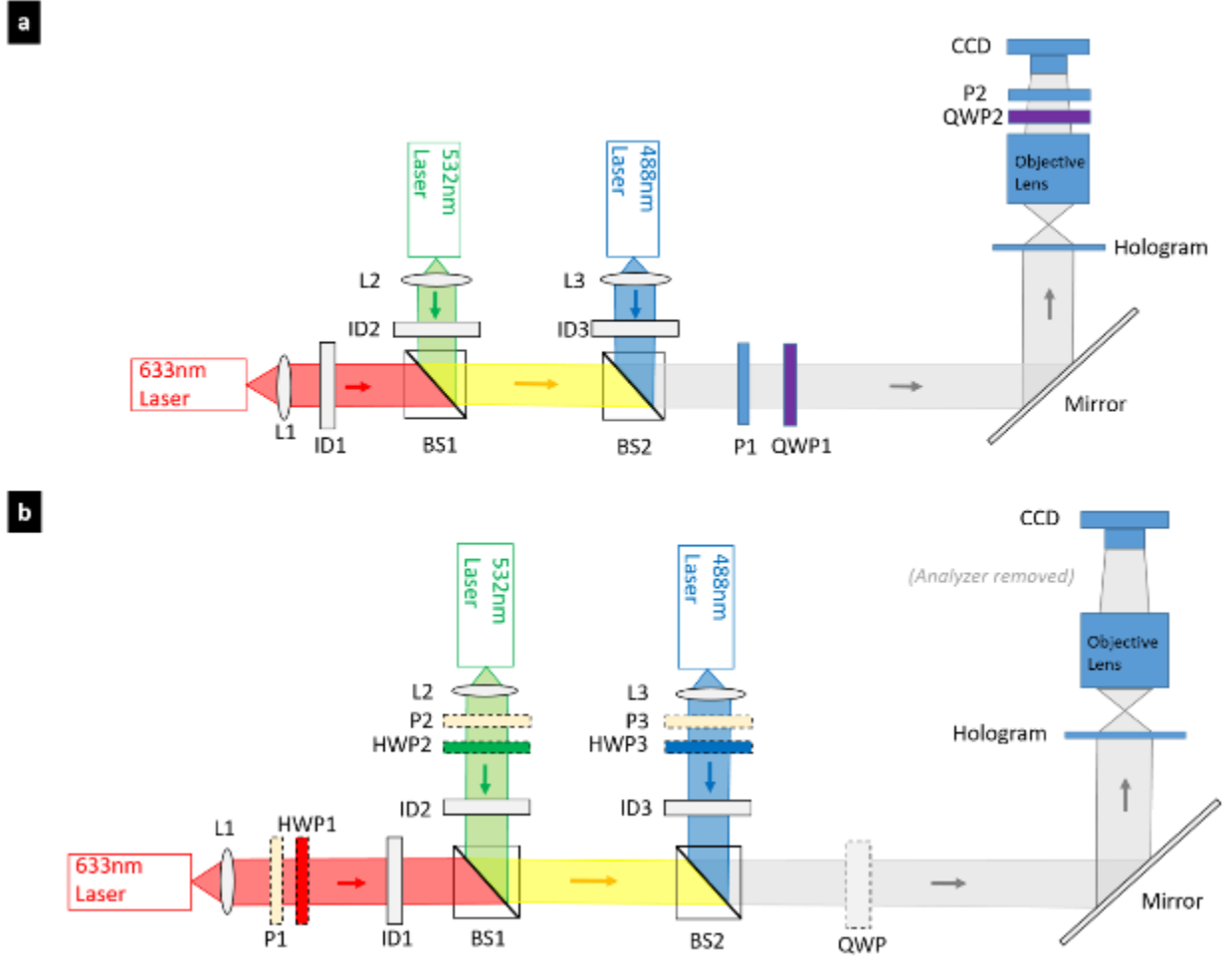


Figure S8. Experimental setup. (a) Experimental setup for the wavelength- and spin-dependent Si hologram imaging. The polarization state for each of the incident laser beams is tuned by controlling the angle between the polarization axis of a polarizer (P) and the fast axis of the quarter-wave plate (QWP). The beams illuminate the metasurface at normal incidence. The reconstructed holographic images are encoded in the transmitted cross-polarized beams, which are collected by a $\times 50$ objective lens with a set of QWP and P before the CCD. Three iris diaphragms (ID1, ID2 and ID3) are used to block or transmit the laser beam at each wavelength. (b) Experimental setup for the measurements of the 6-bit Metasurface. Compared with (a), this setup has three polarizers (P1, P2 and P3) and three half-wave plates (HWP1, HWP2, and HWP3) after the collimated lenses, an achromatic QWP after BSs and does not have a circular polarization analyzer before the CCD

camera (all marked by dash lines). The polarization of the incident beams is tuned by controlling the angle between the fast axis of a half-wave plate (HWP) and the fast axis of the quarter-wave plate (QWP) by rotating the HWP.

S8. Reconstruction of 63 spin- and wavelength-dependent holographic images from the 6-bit metasurface

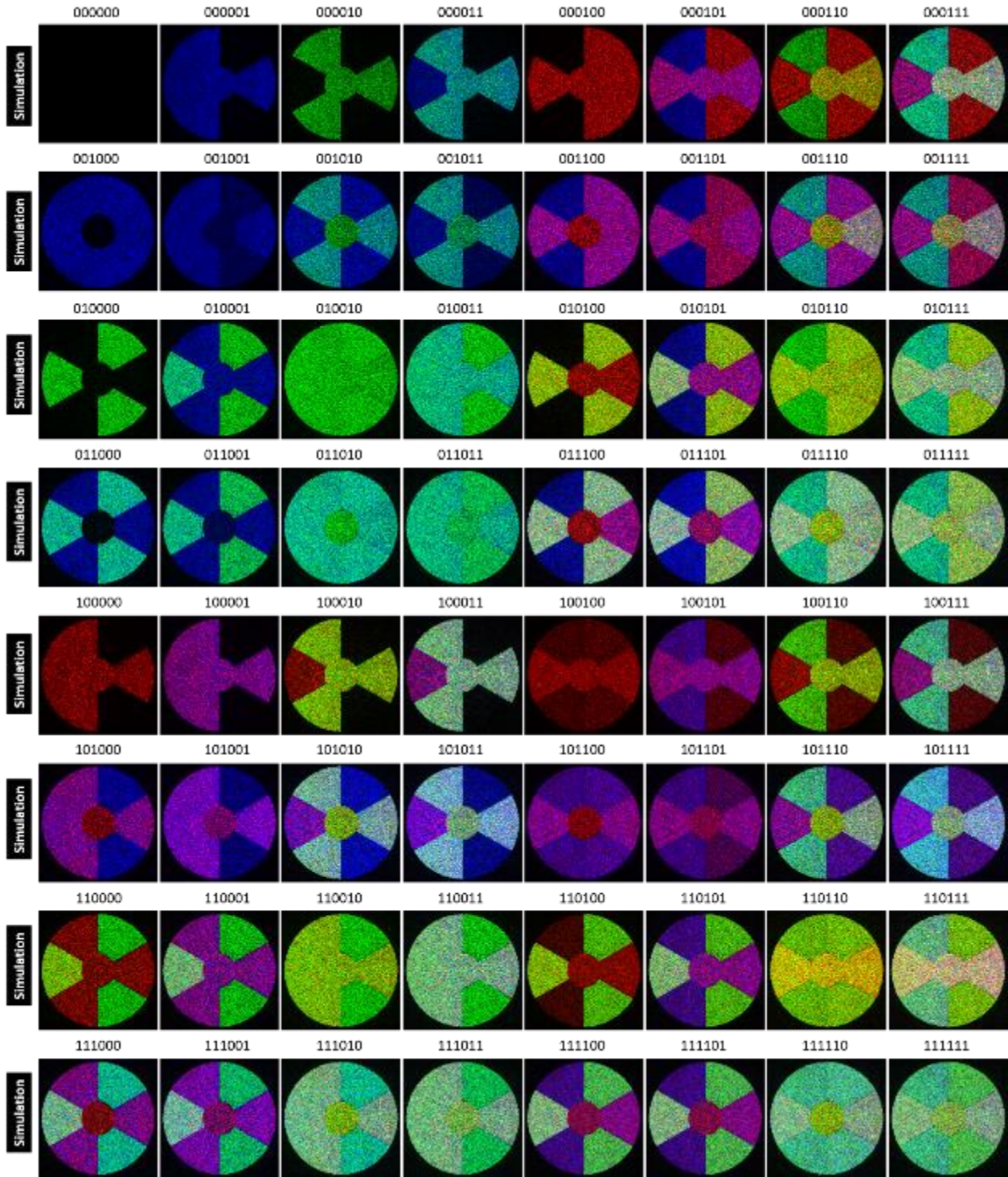


Figure S9. Simulation of the reconstructed intensity profile for the 6-bit metasurface encoding (2^6 -

1) color holograms

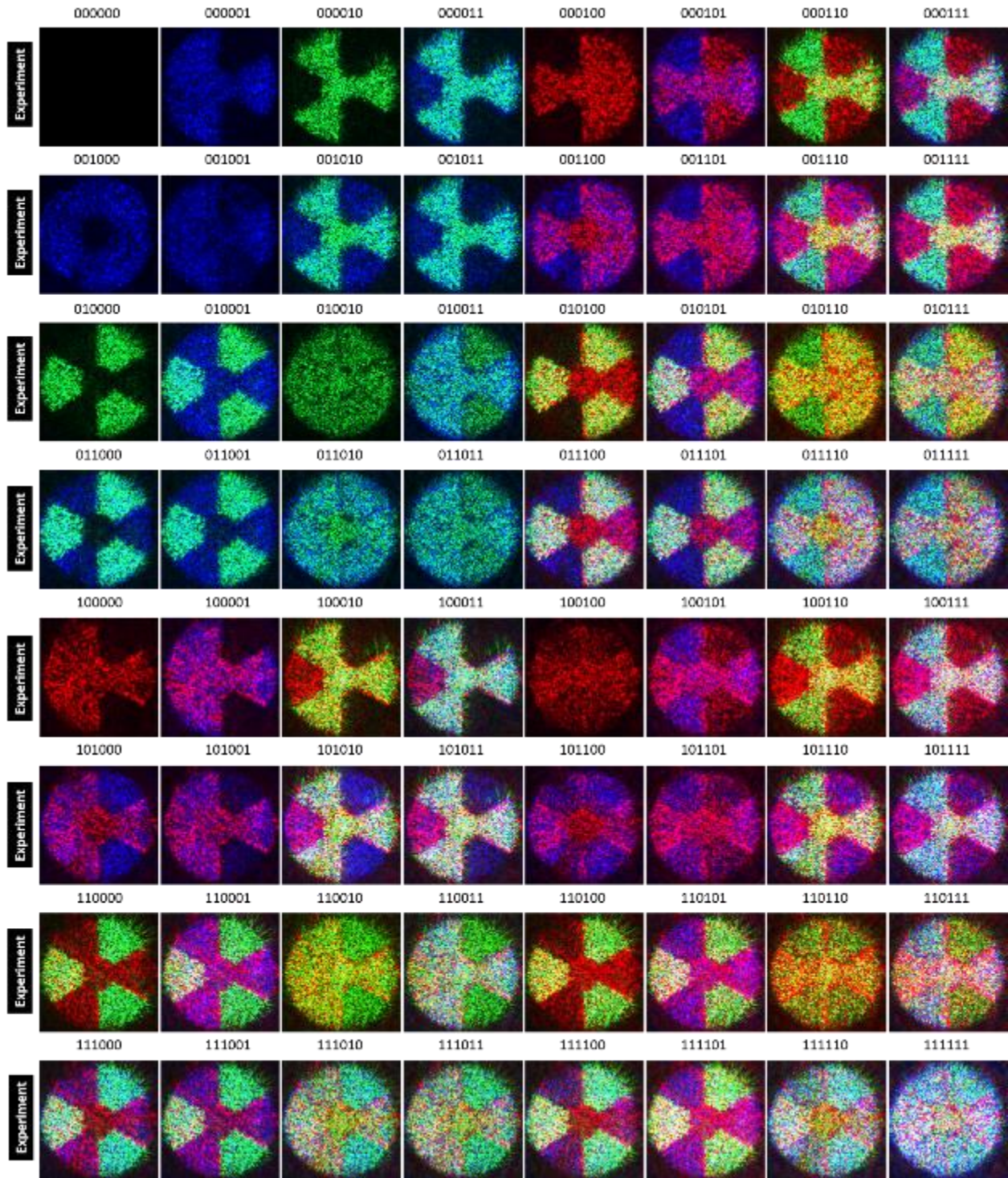


Figure S10. Experimental measurements of reconstructed intensity profile for the 6-bit metasurface encoding (2^6-1) color holograms

S9. Pattern recognition

Figure S11 shows the flow chat of pattern recognition procedure. In this method of pattern recognition, the fundamental bases of measured reconstructed images are known and labelled by $\hat{I}_{r_{RCP}}, \hat{I}_{g_{RCP}}, \hat{I}_{b_{RCP}}, \hat{I}_{r_{LCP}}, \hat{I}_{g_{LCP}}$ and $\hat{I}_{b_{LCP}}$, which correspond to the 6 fundamental bases of the incident beams ($\hat{R}_{RCP}, \hat{G}_{RCP}, \hat{B}_{RCP}, \hat{R}_{LCP}, \hat{G}_{LCP}$ and \hat{B}_{LCP}). The pattern recognition method is implemented as follows.

Step 1) Input a reconstructed colour image which is needed to be identified.

Step 2) Separate this colour image into red, green and blue components ($R(x, y)$, $G(x, y)$ and $B(x, y)$).

Step 3) Count the number of pixels N_R for the red (R) component which intensity is larger than $I_{threshold}$. If $N_R > N_{threshold}$, go to step 4). Otherwise, go to step 6.4).

Step 4) Compute correlations ($Corr_{RCP}$ and $Corr_{LCP}$) between red component $R(x, y)$ and fundamental reconstructed red images $\hat{I}_{r_{RCP}}(x, y)$ and $\hat{I}_{r_{LCP}}(x, y)$. The correlation is the mean of the nonlinear correlation distribution $NC(x, y)$ at the central region. The nonlinear correlation distribution is described by⁽⁸⁾

$$NC_h(x, y) = \left| IFT \left(\left| \{FT[\hat{I}_{r_h}(x, y)]\} \{FT[R(x, y)]\}^* \right|^{p-1} \{FT[\hat{I}_{r_h}(x, y)]\} \{FT[R(x, y)]\}^* \right) \right|^2$$

where $h = RCP$ or LCP ; FT and IFT respectively denote 2D Fourier transform and inverse 2D Fourier transform.

Step 5) Compare $Corr_{RCP}$ and $Corr_{LCP}$ with $Corr_{threshold}$

Step 5.1) If $Corr_{RCP} \& Corr_{LCP} < Corr_{threshold}$ is satisfied, go to Step 6.4),
Otherwise, go to Step 5.2)

Step 5.2) If $Corr_{RCP} \& Corr_{LCP} \geq Corr_{threshold}$ is satisfied, go to Step 6.3),
Otherwise, go to Step 5.3)

- Step 5.3) If $Corr_{RCP} \geq Corr_{threshold}$ is satisfied, go to Step 6.2), Otherwise, go to Step 6.1)
- Step 6) Confirm combination of the fundamental red image bases
- Step 6.1) R is formed by basis \hat{I}_{rLCP} .
- Step 6.2) R is formed by basis \hat{I}_{rRCP} .
- Step 6.3) R is formed by bases \hat{I}_{rRCP} and \hat{I}_{rLCP}
- Step 6.4) R does not contain red colour bases
- Step 7) Repeat Step 3)-Step 6) changing the component and fundamental image bases from red to green, to confirm the combination of the fundamental green image bases.
Then go to Step 8)
- Step 8) Repeat Step 3)-Step 6) changing the component and fundamental image bases from green to blue, to confirm the combination of the fundamental blue image bases.
Then go to Step 9)
- Step 9) Identify the code of the input reconstructed colour image.

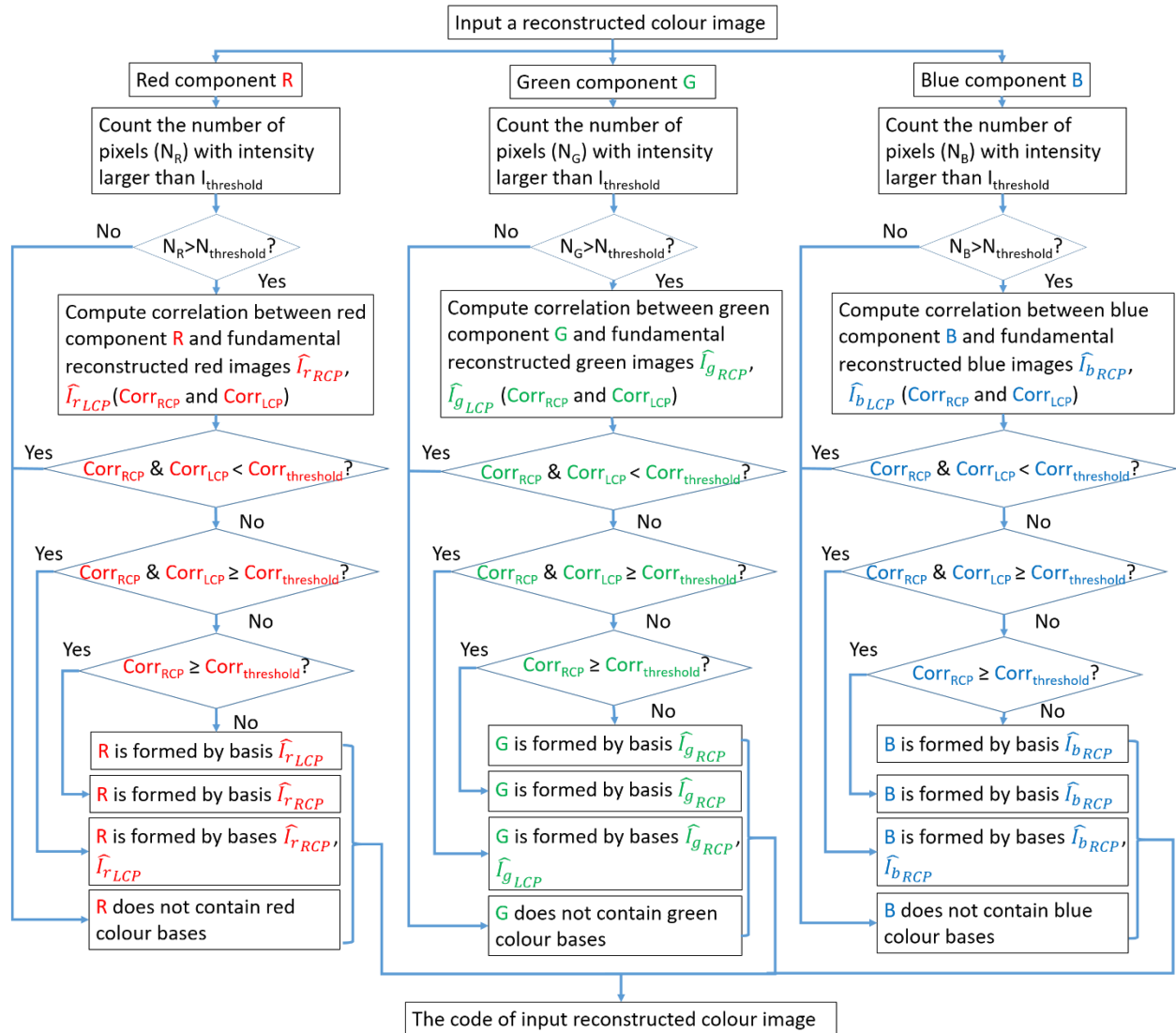


Figure S11. The flow chart of the pattern recognition procedure.

S10 Diffraction efficiency and signal-to-noise ratio

Here, diffraction efficiency and signal-to-noise ratio (SNR) are calculated via Fresnel diffraction. In this calculation, the number of units in a phase profile is fixed at 850×850 . The Arabic numerals 1 to 7 are chosen as the reconstructed images, and working wavelengths are chosen from 400 to 1000 nm with step 100 nm.

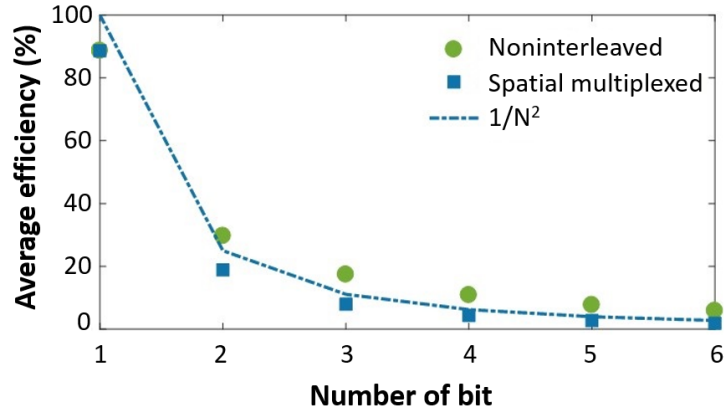


Figure S12. Average diffraction efficiency. The diffraction efficiency is defined as the ratio between the power of the reconstructed monochromatic image and the power of the converted transmitted light.⁽⁹⁾ In this calculation, the reconstructed images of different bits are located at the different areas of the same plane. Noninterleaved phase profile is designed by our method and labelled by “Noninterleaved”. The spatial multiplexed phase profile (labelled by “Spatial multiplexed”) is formed by several spatial multiplexed sub-arrays, and each i^{th} sub-array carries the monofunctional phase profile φ_i retrieved by GS algorithm. Green dots and blue squares denote the average diffraction efficiency of noninterleaved and spatial multiplexed metasurfaces, respectively. The blue dash line corresponds to $1/N^2$.⁽¹⁰⁾ N is the number of bit.

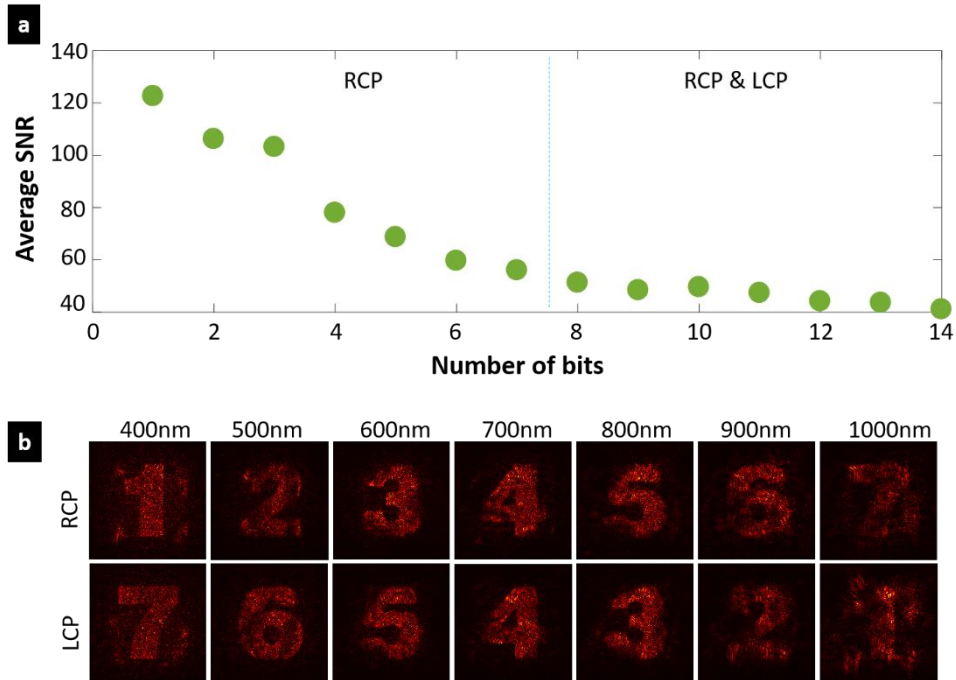


Figure S13. (a) Average signal-to-noise ratio (SNR). The SNR is the peak intensity in the image divide by the standard deviation of the background noise.⁽⁹⁾ In this calculation, the reconstructed images of different bits are located at the same area. The phase profiles are designed by our method. (b) All simulated reconstructions of the 14-bit phase profile.

References:

- (1) Yu, N.; Capasso, F. *Nature Mater.* **2014**, 13(2), 139-150.
- (2) Evlyukhin, A. B.; Reinhardt, C.; Evlyukhin, E.; Chichkov, B. N. *JOSA B*, **2013**, 30(10), 2589-2598.
- (3) Yang, Y.; Miroshnichenko, A. E.; Kostinski, S. V.; Odit, M.; Kapitanova, P.; Qiu, M.; Kivshar, Y. S. *Phys. Rev. B* **2017**, 95(16), 165426.
- (4) Dong, Z.; Ho, J.; Yu, Y.F.; Fu, Y.H.; Paniagua-Dominguez, R.; Wang, S.; Kuznetsov, A.I.; Yang, J.K. *Nano Lett.* **2017**, 17(12), 7620-7628.
- (5) Kerker, M.; Wang, D.-S.; Giles, C.L. *J. Opt. Soc. Am.* **1983**, 73,765-767.
- (6) Gerchberg, R. W.; Saxton, W. O. *Optik* **1972**, 35, 237.
- (7) Chen W. ; Chen X. *J. Opt.* **2011**, 13, 115401.
- (8) Chen W. *IEEE Photocis J.* **2016**, 8, 1.
- (9) Ni, X.; Kildishev, A.V. and Shalaev, V.M. *Nat. Commun.* **2013**, 4, p.2807.
- (10) Maguid, E.; Yulevich, I.; Veksler, D.; Kleiner, V.; Brongersma, M.L. and Hasman, E. *Science*, **2016**, aaf3417.